ENHANCEMENT OF STRESS CORROSION CRACKING OF AZ31 MAGNESIUM ALLOY IN SIMULATED BODY FLUID THANKS TO CRYOGENIC MACHINING

M. Peron [a], R. Bertolini [b], A. Ghiotti [b], J. Torgersen [a], S. Bruschi [b], F. Berto [a]

[a] Department of Industrial and Mechanical Engineering, Norwegian University of Science and Technology, Richard Birkelands vei 2b, 7034 Trondheim, Norway

[b] Department of Industrial Engineering, University of Padova, Via Venezia 1, 35131, Padova, Italy

Abstract

Magnesium and its alloys have recently attracted great attention as potential materials for the manufacture of biodegradable implants. Unfortunately, their inadequate resistance to the simultaneous action of corrosion and mechanical stresses in the human body have hampered their use as implant materials. This work aims at evaluating the Stress Corrosion Cracking (SCC) susceptibility of the AZ31 Mg alloy after being machined under cryogenic cooling. The SCC behaviour was evaluated by means of Slow Strain Rate Tests (SSRTs) in Simulated Body Fluid (SBF) at 37 °C. Prior to testing, a full characterization of the machined surface integrity, including microstructural observations, residual stress, nano-hardness measurements and surface texture analysis was carried out together with the assessment of the corrosion properties through potentiodynamic polarization curves. In addition, the morphology of the fracture surfaces after SSRTs was analysed by means of 3D optical profiler and Scanning Electron Microscopy (SEM). The improved corrosion resistance due to the increased extension of the nano-surface layer and to the compressive residual stresses represents the reason of the reduced SCC susceptibility of cryogenically machined AZ31 samples as compared to dry machined ones.

Keywords

1. Introduction

During the past years life expectancy has been continuously increasing, leading to an incessant growing number of people undergoing surgical procedures involving the implantation of medical devices [1]. Among these procedures, the orthopaedic sector experiences the highest growth. In Australia, for example, bone fractures represent about 54% of the injury hospitalisations [2]. The materials currently used in orthopaedic surgery are permanent metallic materials, such as stainless steel, titanium, and cobalt-chromium alloys [3]. Because of their high strength and good corrosion resistance, they have been widely used as load-bearing implants for bone healing and repair of damaged tissues [4–6]. The key problems with these permanent implants are however two-fold. Firstly, the great difference in elastic modulus of these materials compared to that of human bone results in the occurrence of the stress-shielding phenomenon. This is a consequence of stress distribution changes between the bone and the implant [7–13]: bones adapt to the reduced stress field according to the Wolff's law [14], resulting in the bone either becoming more porous (internal remodelling) or thinner (external remodelling), increasing the possibility of implant failure. Secondly, due to the arise of long-term complications [15–19], the permanent implant must be removed when the healing process is completed. However, the additional surgeries necessary to remove the implant cause an increase in costs to the health care system, as well as emotional stress to the patient. In order to solve these drawbacks, biodegradable metallic materials have been studied, in particular Mg and its alloys [20–22]. Mg has in fact low density and an elastic modulus in mechanical compatibility with natural bone, minimizing the risk of the stress shielding phenomenon [20]. In addition, Mg is highly abundant in the human body [23]. Indeed, it is

essential for the metabolism in many biological mechanisms, being a cofactor for many enzymes [24], and Mg^{2+} ions resulting from the degradation process are reported to aid the healing process and the growth of tissue. Despite their highly attractive properties, Mg and its alloys have not yet been used as implant materials because of their high corrosion rates in physiological environments, which may result in a loss of mechanical integrity and in hydrogen evolution at a rate that is too fast for the bone tissue to accommodate. In addition, in orthopaedic applications, the implant must possess adequate resistance to failure when the corrosive human body fluid acts concurrently with the mechanical loading characteristics of the human body. Corrosion-assisted cracking phenomena, such as stress corrosion cracking (SCC) and corrosion fatigue (CF), were in fact reported to cause the failure of several traditional implants [25–28]. In particular, SCC is particularly dangerous because it leads to a sudden and catastrophic failure under mechanical loadings otherwise considered safe, and Mg and its alloys are particularly susceptible [29–31]. Therefore, it is important to develop Mg-based implants granting both strength and corrosion resistance in the human body without causing corrosion-assisted cracking phenomena.

Most studies focused on improving their electrochemical properties, whereas improving their resistance to corrosion-assisted cracking is overlooked. In fact, while different procedures have been applied in recent years to improve their corrosion resistance (alloying, surface modification, …), yet few of them have been assessed regarding their effects on the susceptibility to corrosion-assisted cracking phenomena. Mohajernia et al. [32] reported that hydroxyapatite coating containing multi-walled carbon nanotubes reduced the corrosion current density of AZ31 alloys by three orders of magnitude. In addition, they reported the elongation to failure of AZ31 samples subjected to slow strain rate tests (SSRT) in simulated body fluid (SBF) at 37 °C to be increased about 70% with the application of the coating. These results agree with those obtained by Chen et al. [33]. The authors coated Mg-4Zn-0.6Zr-0.4Sr with a composite coating consisting of a poly (lactic-co-glycolic acid) (PLGA) superimposed to a micro-arc oxidation (MAO) layer and they reported this composite coating to increase the elongation to failure of the bare alloy subjected to SSRT in modified simulated body fluid (m-SBF) at 37 °C from 5% to 11%. Again, the corrosion rate was reduced by three orders of magnitude. However, when cyclic loading is applied, the presence of coatings might result to be detrimental for the fatigue life of the implants due to the formation of cracks in the coating (due to elastic modulus mismatch) that acts as stress concentrators and also due to the generally higher surface roughness of the coated samples compared to the polished uncoated counterparts [34]. Alternatively, alloying has been reported as a valuable solution to improve the corrosion resistance of Mg and to mitigate the corrosion-assisted cracking phenomena. For instance, Kannan et al. [35], compared the SCC susceptibility of three different rare earth (RE)-containing alloys, namely ZE41, QE22 and EV31A, with that of AZ80 alloy. They suggested that rare-earth elements in Mg alloys can improve the SCC resistance significantly, being EV31A alloy the most resistant to SCC compared to the other alloy. The beneficial effect of RE was found also by Choudhary et al. [36]. According to their findings, a lower SCC susceptibility was observed for RE-containing alloys, i.e. WZ21 and WE43 compared to Mg-Zn-Ca alloy (ZX50). However, some RE elements were reported to be toxic for the human body [37], and in general alloying may introduce elements that lead to adverse biological reactions. In recent years, mechanical processing inducing severe plastic deformation (SPD) have been investigated as an alternative to alloying and coating techniques. Again, broad attention was given to the effect of SPD techniques on the corrosion properties, whereas very few on the SCC susceptibility. Equal channel angular pressing (ECAP) has been extensively studied as method to reduce the corrosion rate due to its capability to induce a very fine and homogeneous microstructure. Sunil et al. [38] reported a better degradation behaviour of AZ31 alloy after four passes of ECAP compared to the annealed counterparts. These results agree with those obtained by Zhang et al. [39], where a decrease in the corrosion current density was obtained increasing the number of passes of ECAP. In addition, ECAP treated AZ61 alloys were reported to be characterized by an elongation to failure 30% higher than the as-cast material [40]. However, conventional SPD techniques such as ECAP require multiple deformation passes to accumulate large strain in the material, and suitable processing routes are also necessary to refine the material

microstructure down to ultrafine grains [41]. Recently, machining has been studied as an effective method to achieve SPD. In fact, compared with the conventional SPD techniques, machining has been reported to impose higher level of strain into the workpiece material in just a single stage operation [42]. Furthermore, the use of liquid nitrogen as coolant during turning has recently shown to further improve the functional performance and product life [43]. Orthogonal cutting trials with different cutting tools with two edge radii were carried out under both dry and cryogenic conditions in [44]. Results showed that cryogenic machining using a large edge radius tool led to a thicker grain refinement layer, larger compressive residual stresses, and stronger intensity of basal texture compared to the dry machined condition. The effect of the improved surface integrity on corrosion resistance was evaluated by the same Authors in [45], in which optical inspection of the machined surfaces after immersion in saline solution was evaluated. It was stated that the degree of corrosion was correlated with the extension of the sub-surface featureless layer formed after turning: since cryogenic machining maximized the thickness of the layer, it led to the best corrosion behaviour. A step forward was made by Bruschi et al. [46], who investigated the effect of feed and cooling conditions on the corrosion resistance of the machined AZ31 Mg alloy. The corrosion resistance was measured through potentiodynamic polarization curves in Simulated Body Fluid (SBF) at body temperature. A reduction up to an order of magnitude in the corrosion current density was found in the case of cryogenic machining regardless of the adopted feed. These improvements were associated to a wider nano-crystalline layer formed on the surface along with the generation of a more compressed surface.

These findings show that cryogenic machining is a viable path forward, but the mechanisms by which the SCC resistance improves, i.e. the microstructural reasoning behind such gains in performance, remain yet to be discovered. Here, AZ31 samples were machined under cryogenic cooling, and afterwards subjected to Slow Strain Rate Tests (SSRTs) at a strain rate of $3.5 \cdot 10^{-6}$ s^{-1}. The samples were immersed for the whole duration of the tests in SBF at 37 °C. The behaviour of dry machined samples was also investigated as a reference, reporting a higher SCC susceptibility. In support to a complete understanding of the different behaviour shown by dry and cryogenically machined samples, the authors carried out a full characterization of the surface integrity, including microstructural observations, residual stress, nano-hardness measurements and surface texture analysis, an evaluation of the corrosion behaviour through potentiodynamic polarization curves, and an analysis of the fracture surfaces after SSRTs with a Scanning Electron Microscope (SEM) and a 3D optical profiler.

2. Materials and methods

2.1. Material

AZ31 magnesium alloy was supplied in form of commercially available bars. The samples were cut and prepared for microstructural analysis using SiC papers for grinding and colloidal silica for final polishing. The grain structure was revealed by etching using a solution of alcohol (95 ml), picric acid (5 g), and acetic acid (10 ml) for 10 s. The microstructure was examined using a Leica DMRE™ Optical Microscope (OM). The microstructure of the material in the as-received condition is shown in Figure 1 and consists of a quite homogeneous α matrix. The initial grain size was measured by linear intercept method and resulted equal to 24.1 ± 4 μm.
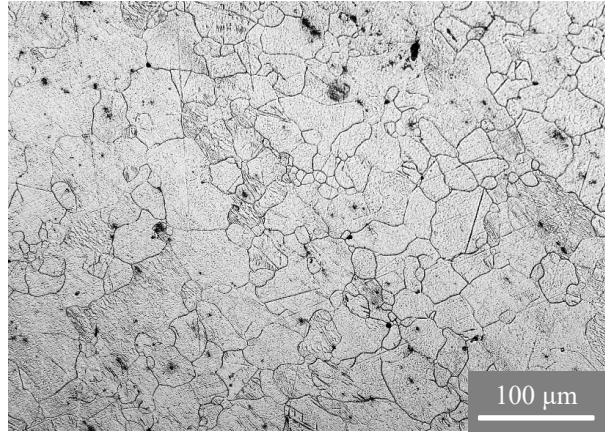
Figure 1. Microstructure of the AZ31 alloy in the as-received condition.

2.2. Machining tests

To carry out SSRTs, cylindrical dog-bone-shaped samples, whose dimensions are reported in Figure 2 a, were used according to the standard [49]. The samples were machined on a Mori Seiki NL 1500™ CNC lathe equipped with an experimental setup devoted to the delivery of liquid nitrogen, specifically designed and described in detail in a previous work by the Authors [47], and herein reported in Figure 2b. To obtain the dog-bone shape of the samples, the machining operations were subdivided into two steps, namely a roughing and a finishing pass. For the roughing pass, the following machining parameters were employed: depth of cut (d) equal to 1 mm, cutting speed (Vc) of 80 m/min, and feed (f) equal to 0.2 mm/rev, whereas for the finishing pass the parameters were: depth of cut equal to 0.25 mm, a cutting speed of 100 m/min, and a feed equal to 0.1 mm/rev.

The surface integrity and corrosion performances after machining were evaluated on cylindrical samples manufactured using the same machining parameters applied for the realization of the dog-bone samples.

During all the machining operations, the workpiece was grabbed by the counter spindle of the lathe with a pressure of 1.30 kN to avoid vibrations.
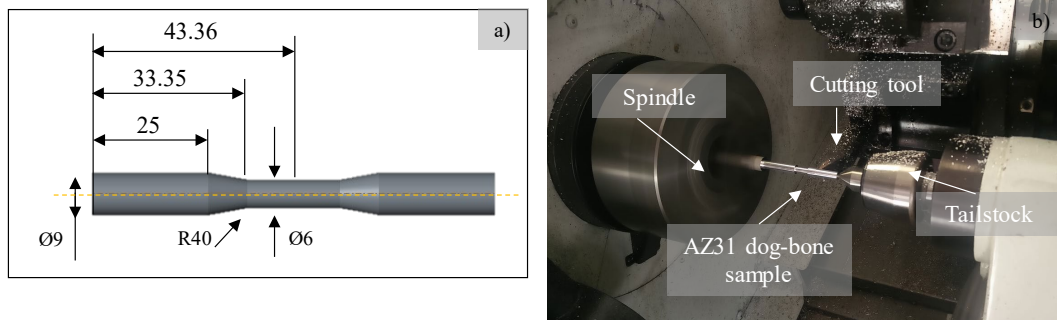

Figure 2. (a) Geometry and dimensions of the samples for SSRTs; (b) Experimental setup for the realization of the dog-bone samples in dry condition.

2.3. Surface integrity characterization

After machining, the cylindrical samples were cut along their section and prepared for microstructural characterization using the same procedure described in §2.1. The measurements of the machining-induced Severe Plastic Deformed (SPD) layers were carried every each 10 μm on three different OM images at 1000X magnification.

Samples were also extracted from the machined workpieces for Transmission Electron Microscopy (TEM) analysis and nano-hardness measurements. The cross-sectional TEM samples were prepared using a FEI™ Nova 200 dual-beam Focused Ion Beam (FIB) system. The TEM lamellas were then ion-milled with a 30 kV beam and finally polished at 5 kV. After reaching a thickness of ~100 nm, a Fischion™ NanoMill was used to further clean the FIB damaged surface at both sides. Selected Area Diffraction (SAD) and Bright Field (BF) TEM imaging were performed at 300 keV using a Hitachi™ HF3300 TEM.

The nano-hardness at the surface of the machined samples was measured with a diamond Berkovich indenter tip using the Hysitron™ TriboIndenter 800 load- and depth-sensing nano-indenter system [8]. A minimum of 20 nano-indentations was performed for each sample with a maximum load of 5 mN and data acquisition frequency of 5 Hz.

The residual stresses were determined with CuKα-radiation using the (2,1,3) interference lines. The measurements were performed using a Spider™ X GNR portable diffractometer working at 30 KV and 90 μA. The analysis was based on the sin2ψ-method for which the lattice spacings d were measured at five ψ-angles between −35° and +35°. For the calculation of residual stresses at the characterization site, Young's modulus and Poisson's ratio were assumed to be 45 GPa and 0.25, respectively. The counting time for each of the five measures at different ψ-angles was 500 s. The depth distribution of the residual stresses was determined by electrolytic removal of thin surface layers and subsequent X-ray measurements. For electrolytic polishing, we used a solution of 90 ml of water, 730 ml of ethanol, 100 ml of butoxyethanol and 78 ml of perchloric acid working at 18 V for 30 s at 20°C.

The machined surface textures were measured using a Sensofar™ Plu-Neox optical profiler with a 20x magnification Nikon™ confocal objective. To inspect surface defects, confocal images were acquired with the same objective.

2.4. Corrosion performances evaluation

Potentiodynamic polarization tests were carried out on an Amel™ 2549 potentiostat, making use of a standard three-electrodes cell, where the machined cylindrical samples were the working electrode, a saturated Calomel electrode (SCE) the reference electrode, and a platinum electrode the counter electrode. The samples were immersed in SBF solution, whose composition is reported in Table 1. The temperature was set to 37±1°C to reproduce the human body conditions. The potentiodynamic polarization curves were obtained applying a potential from -2 V to -1.3 V at a scan rate of 0.5 mVs^{-1}. The corrosion potential and corrosion current density were determined using the Tafel extrapolation method, according to the ASTM G5-14 standard. The tests were repeated three times for each machining condition.

Reagents	Amount
NaCl	8.035 g
NaHCO$_3$	0.355 g
KCl	0.225 g
K$_2$HPO$_4\cdot$3H$_2$O	0.231 g
MgCl$_2\cdot$6H$_2$O	0.311 g
1.0$_M$-HCl	39 ml
CaCl$_2$	0.292 g
Na$_2$SO$_4$	0.072 g
Tris	6.118 g

Table 1. Reagents and their quantities for preparation of 1000 ml of the SBF solution according to [48].

2.5. Slow strain rate tests (SSRT)

The SSRT experiments were carried out on the machined dog-bone samples at a strain rate of $3.5 \cdot 10^{-6}$ s^{-1} in SBF solution at body temperature ($37 \pm 1°C$). The strain rate value was chosen in order to make the AZ31 alloy susceptible to SCC according to [35]. A schematic representation of the experimental set-up is shown in Figure 3. The sample was immersed for the whole duration of the test and the SBF solution was constantly changed by means of a pumping system. The SBF solution container was immersed in a water bath, whose temperature was constantly monitored by a thermometer. When the temperature was below its set value, a commercial resistance heating element placed inside the water bath automatically turned on until the desired temperature was reached again. In addition, while carrying out the SSRTs, the area of the specimen exposed to SBF was restricted to its gauge length using Teflon tapes wrapping the rest of the specimen, thus maintaining a constant area of exposure to the corrosive solution as well as avoiding the possibility of galvanic effect with other components of the testing set-up. For sake of comparison, also SSRTs in air were carried out.
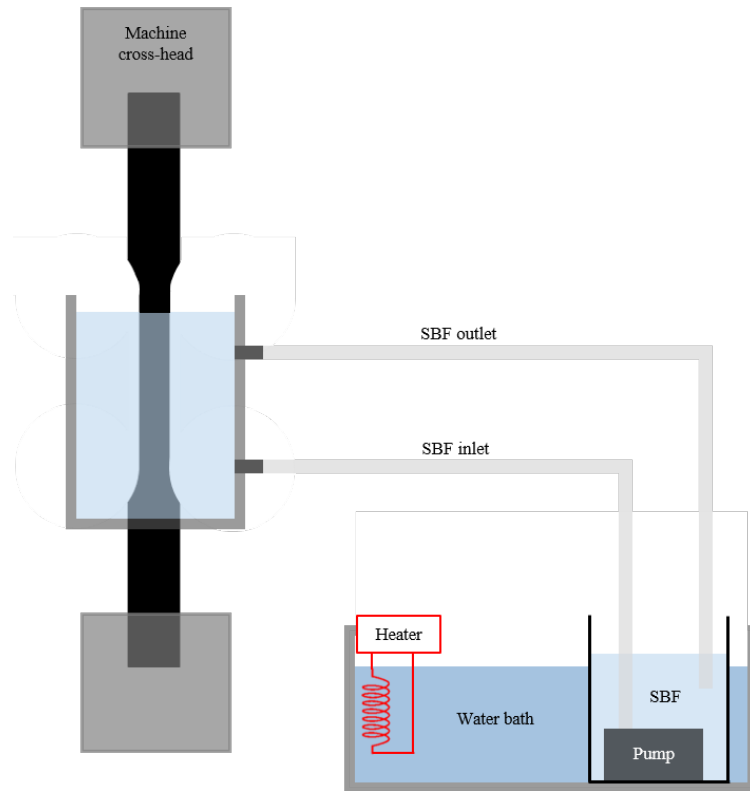

Figure 3. Schematic representation of the SSRT set-up.

The samples were cleaned with ethanol prior to testing. It is worth noting that, differently from other works on this field [29,31,49], the gauge length of the specimen was not grounded prior to testing, in order to avoid the removal of the surface features induced by the cryogenic machining. SSRTs were repeated three times for reproducibility.

In order to quantify the AZ31 SCC sensitivity, the susceptibility indices I_{UTS} and I_ε were calculated according to Eq. (1) and Eq. (2) [36]:

$$I_{UTS} = \frac{UTS_{air} - UTS_{SBF}}{UTS_{air}} \tag{1}$$

and

$$I_\varepsilon = \frac{\varepsilon_{air} - \varepsilon_{SBF}}{\varepsilon_{air}} \qquad (2)$$

where *UTS* is the Ultimate Tensile Strength and ε the elongation at failure, both evaluated during tests conducted in SBF solution and air. When the value of the susceptibility index approaches zero, the material is considered to be highly resistant to SCC, namely the greater the index the greater the susceptibility to SCC.

2.6. Characterization after SSRT

The specimen fracture surfaces after SSRTs were cleaned by immersion for one minute in a solution prepared using 50 g chromium trioxide (CrO_3), 2.5 g silver nitrate ($AgNO_3$) and 5 g barium nitrate ($Ba(NO_3)_2$) in 250 ml distilled water, as suggested by [50]. The specimens were then washed with distilled water and finally ultrasonically cleaned in acetone for 10 min. The fracture surfaces were observed by means of a FEI™ QUANTA 450 SEM in Secondary Electron (SE) mode. The topography of the surface fractures was also measured using a Sensofar Plu Neox™ with a confocal 20X objective.

Finally, the fractured specimens were cut along their longitudinal section. The microstructure was observed by using the same experimental approach described in § 2.1.

3. Results

3.1. Surface integrity

Figures 4a and 4b show the micrographs of the samples machined under dry and cryogenic conditions, respectively. From these images, it can be seen that machining introduced an SPD layer close to the surface irrespective of the cutting conditions. Such layers consisted of ultrafine grains highly deformed along the cutting direction, characterized also by the presence of slip bands. The extension of the SPD layer increased by 24% with cryogenic cooling compared to dry cutting.
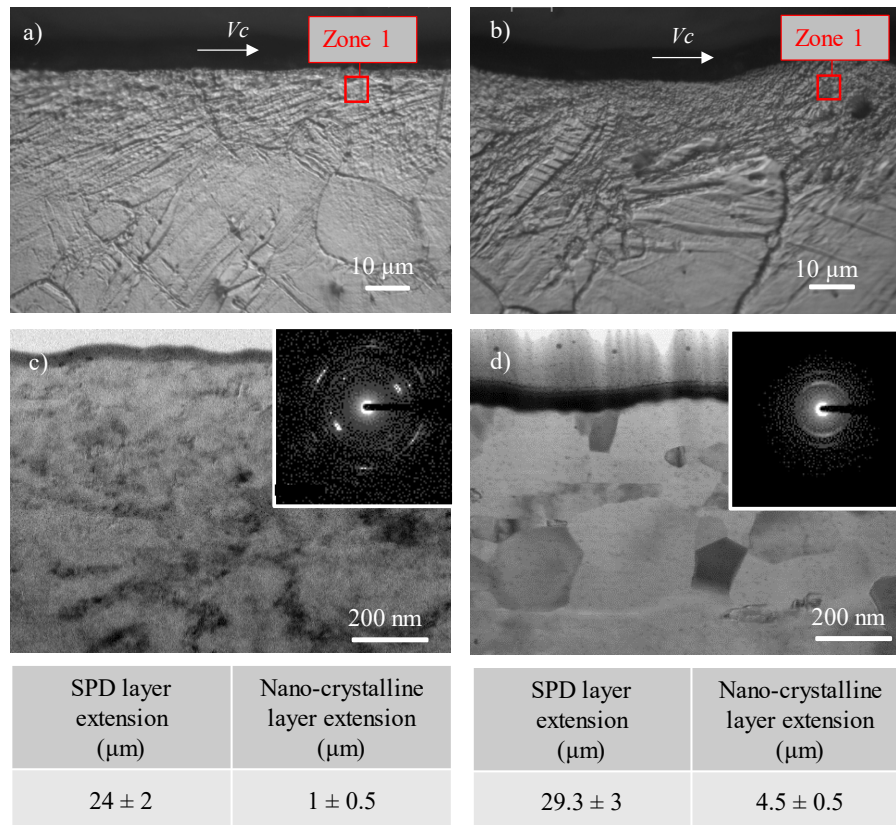
SPD layer extension (μm)	Nano-crystalline layer extension (μm)	SPD layer extension (μm)	Nano-crystalline layer extension (μm)
24 ± 2	1 ± 0.5	29.3 ± 3	4.5 ± 0.5

Figure 4. Optical images (a and b), BF TEM micrographs and SAD patterns (c and d) of the dry (on the left) and cryogenic (on the right) machined samples.

To further characterize the SPD layers, high-magnification TEM bright field images were captured on Zone 1 of Figure 4 a and b and shown in Figure 4 c and d.

In both cases, a grain refinement upon a nanoscale was achieved, but its extension depended heavily on the cooling condition. In the case of cryogenic machined samples, the nanoscale layer was almost five times thicker than in the dry cut samples. In fact, the SAD pattern of the dry cut samples revealed the presence of micrometre sized grains just below the nanolayer. On the contrary, the SAD pattern of the cryogenic cooled samples assumed a ring-like shape since the nanoscale layer was much wider.

As a consequence of the different microstructural features close to the machined surface, the mechanical properties of the material were altered. The nano-hardness values measured at the machined surface showed a very significant increase compared to the bulk value (1.35 GPa), achieving the values of 2.09 ± 0.5 GPa for the dry samples and 2.12 ± 0.2 for the cryogenic cooled ones. Coherently, no sensible differences in nano-hardness were found between the dry and cryogenic cooled samples since both showed the presence of the nanoscale layer at the machined surface (see Figure 4).

Figure 5 reports the axial residual stresses as a function of the distance from the machined surface. A totally compressive residual stress was found in the case of cryogenic cooling condition, while a tensile residual stress state was found in the case of dry cutting. Actually, the peak of residual stress was 270 MPa (tensile) in dry condition, and decreased to -143 MPa (compressive) in cryogenic condition. After approximately 200 μm from the machined surface, a null state of stress was achieved regardless of the adopted cooling condition.
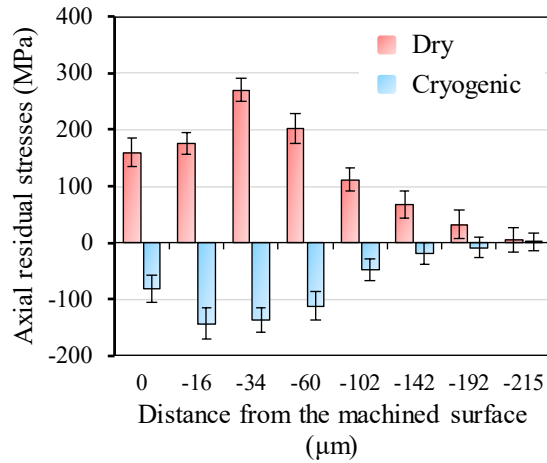
Figure 5. Axial residual stresses as a function of the cooling strategy.

Figure 6 shows the confocal images of the two surfaces machined using the two adopted strategies: no relevant differences can be seen in terms of average surface roughness *Sa* as a consequence of the application of liquid nitrogen during cutting. However, the density of tears was drastically increased in the case of dry cutting. It is worth nothing that the presence of defects is usually not revealed by surface roughness measurements [51].
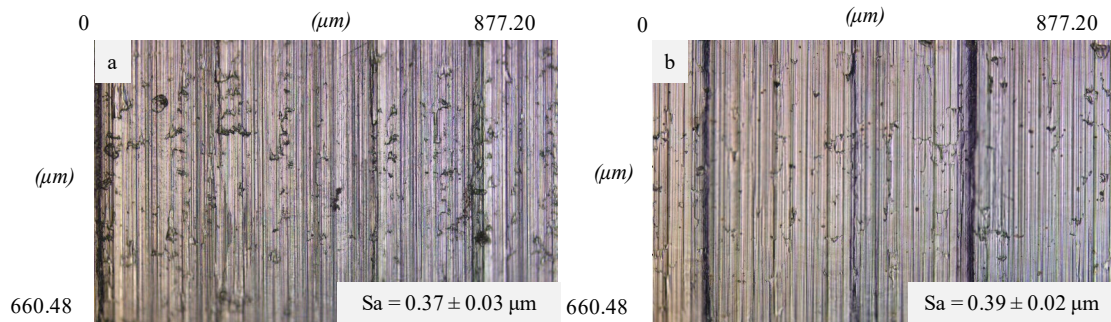

Figure 6. Machined surfaces images and relative surface roughness.

3.2. Corrosion behaviour

The potentiodynamic polarization curves of the AZ31 cylindrical samples plotted on a semi-logarithmic scale are shown in Figure 7. The related kinetic and thermodynamic corrosion electrochemical characteristics are reported in Table 2. Compared to the dry condition, cryogenically machined samples showed an improved corrosion resistance, namely an ennoblement of corrosion potential E_{corr} and a reduction of corrosion current density i_{corr} of an order of magnitude. It is worth noting that the corrosion current density is directly related to the corrosion rate by the Faraday's law, which expresses the material loss of the implant during its permanence into the human body. This implies that the application of liquid nitrogen during cutting leads to a reduced corrosion rate.
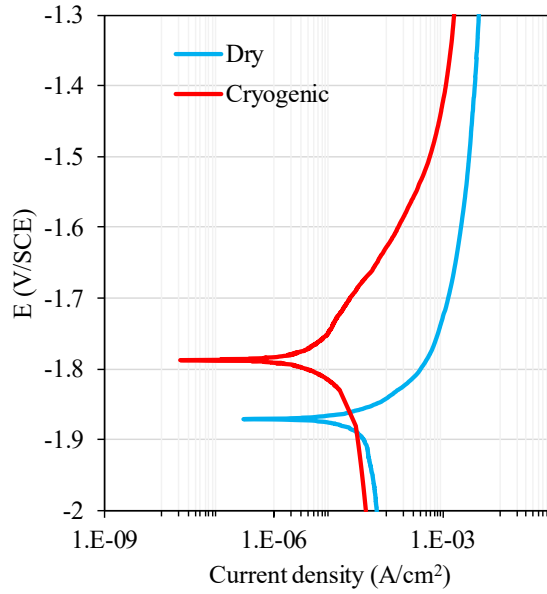
Figure 7. Potentiodynamic polarisation curves for the AZ31 cylindrical samples in SBF solution at 37°C.

	Ecorr (V/SCE)	Icorr (µA/cm^2)
Dry	-1.87 ± 0.015	10 ± 4
Cryogenic	-1.79 ± 0.025	2 ± 0.5

Table 2. Electrochemical corrosion data extrapolated from Figure 6.

3.3 Stress corrosion cracking behaviour

The engineering stress-strain curves for the dry and cryogenic machined AZ31 samples tested in air and in SBF are reported in Figure 8 a and b, respectively. In addition, Table 3 compares the UTS and elongation at failure values obtained from the curves in Figure 8.
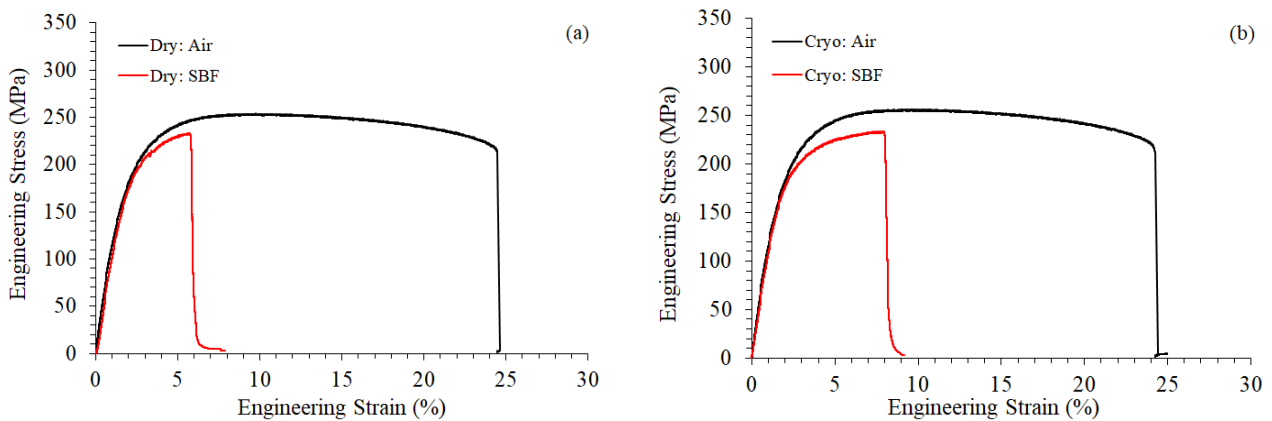

Figure 8. Engineering stress-strain curves of dry (a) and cryogenic (b) machined AZ31 samples tested in air and SBF at 37°C and strain rate of $3.5 \cdot 10^{-6}$ s^{-1}.

Manufacturing strategy	In Air		In SBF	
	UTS (MPa)	Elongation at failure (%)	UTS (MPa)	Elongation at failure (%)
Dry	256.3± 8.7	24.5 ± 0.7	233.3 ± 1.9	6.1 ± 0.3
Cryogenic	253.6± 5.6	24.2 ± 0.5	235.3 ± 1.0	7.8 ± 0.2

Table 3. Mechanical properties from Figure 4.

The machining cooling strategy did not influence the AZ31 mechanical properties when tested in air, since the mechanical behaviour of both dry and cryogenic machined samples is characterized by an elasto-plastic behaviour which resemble the one found by [52]. On the other hand, the considerably reduced elongation at failure when testing in SBF indicates that the alloy suffered embrittlement in SBF regardless of the adopted cooling strategy during cutting. It is however worth noting that cryogenic cooling led to a less pronounced reduction of elongation at fracture compared to the case of dry cutting.

To quantify the SCC susceptibility of the dry and cryogenic-machined samples, the I_{UTS} and I_ε indices were evaluated and are reported in Figure 9.
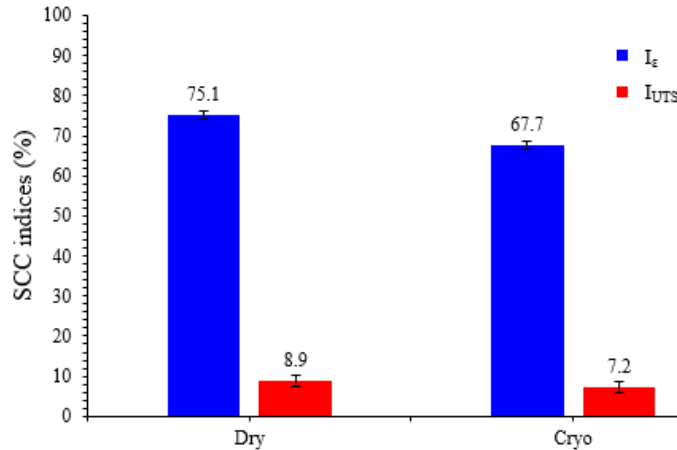

Figure 9. SCC indices for the dry and cryogenic machined samples.

The SCC indices of the cryogenic machined sample are, in general, lower than the ones of the dry machined sample. However, the I_{UTS} and the I_ε values for the dry machined sample are almost 23% and 11% higher than those of the cryogenic machined sample, respectively. This suggests that a higher resistance to SCC in SBF is provided when AZ31 is machined under cryogenic cooling which will be further analysed in section 4.

3.4 **Fracture surfaces**

Figure 10 shows the macroscopic appearance of the cryogenic machined samples after SSRTs. Clearly, the fracture in air exhibits rougher features typical of a ductile fracture; on the contrary, the samples tested in SBF appear smooth and characterized by secondary cracked zones.
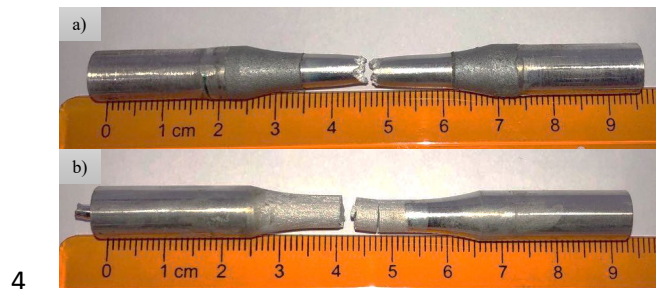

4

Figure 10. Photos of the cryogenic machined samples after SSRTs in: a) air; b) SBF at body temperature.

A more detailed investigation is given in Figure 11, which reports the surface topographies and SEM images of the samples of Figure 10. The overall view of the fracture surface confirms the ductile nature of the failure

in the case of air testing, characterized by a significant amount of dimples, while the sample tested in SBF shows mix mode fracture features, namely ductile and brittle fracture characteristics. An additional confirmation of that is given by the z-range of the height of the surface texture shown in Figure 11 a and d, which is considerably higher in the case of air testing, in relation to a more ductile behaviour.

Finally, the surface fracture appearance is completely different: in the case of SBF condition, both transgranular and intergranular cracks are evident, which are absent in the case of air testing (compare Figure 11 f with Fig. 11 c).

It is worth underlining that these considerations about the fracture features after testing in air and SBF are true irrespective of the adopted cooling conditions and, for the sake of brevity, the outcomes from the dry machined samples are not reported here.
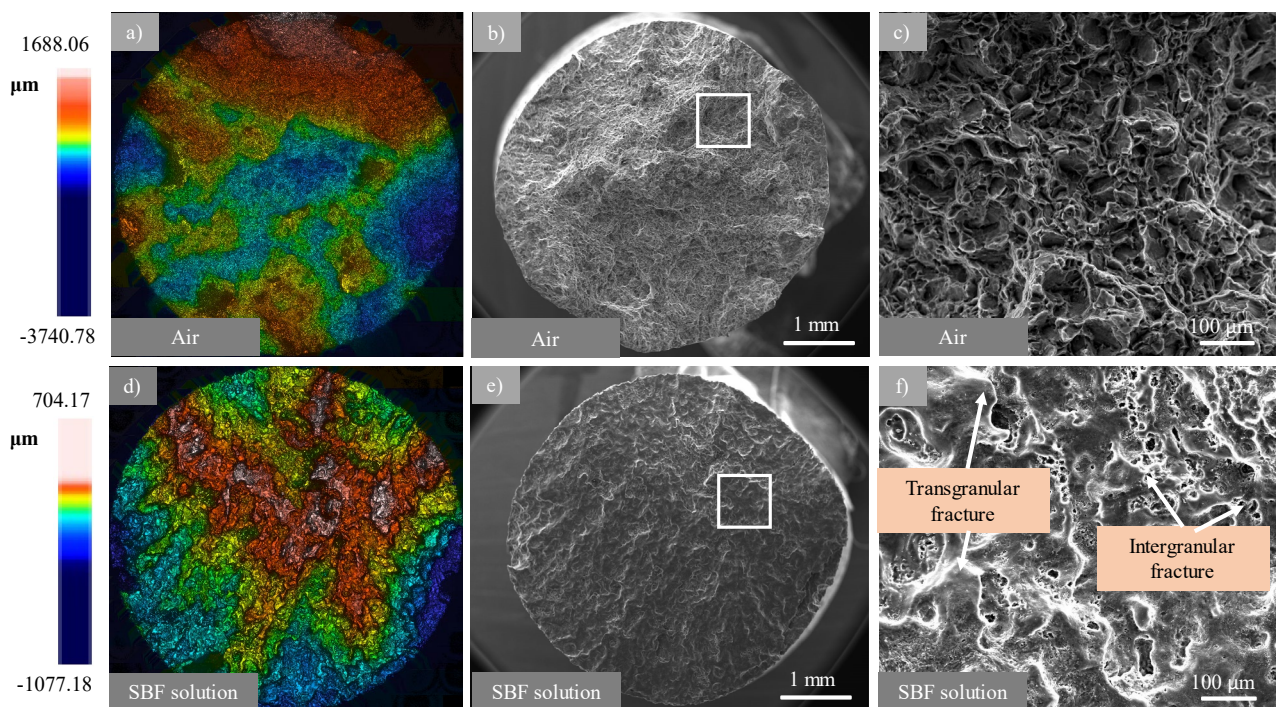

Figure 11. AZ31 samples after cryogenic machining and SSRT in air and SBF: (a) and (d) topographies of the overall fracture surface; (b) and (e) SEM images of the overall fracture surface; (c) and (f) magnified images of the zones highlighted in (b) and (e).

Figure 12. AZ31 samples after dry and cryogenic machining and SSRT in SBF at 37°C: (a) and (d) topographies of the overall fracture surface; (b) and (e) SEM images of the overall fracture surface; (c) and (f) magnified images of the zones highlighted in (b) and (e).
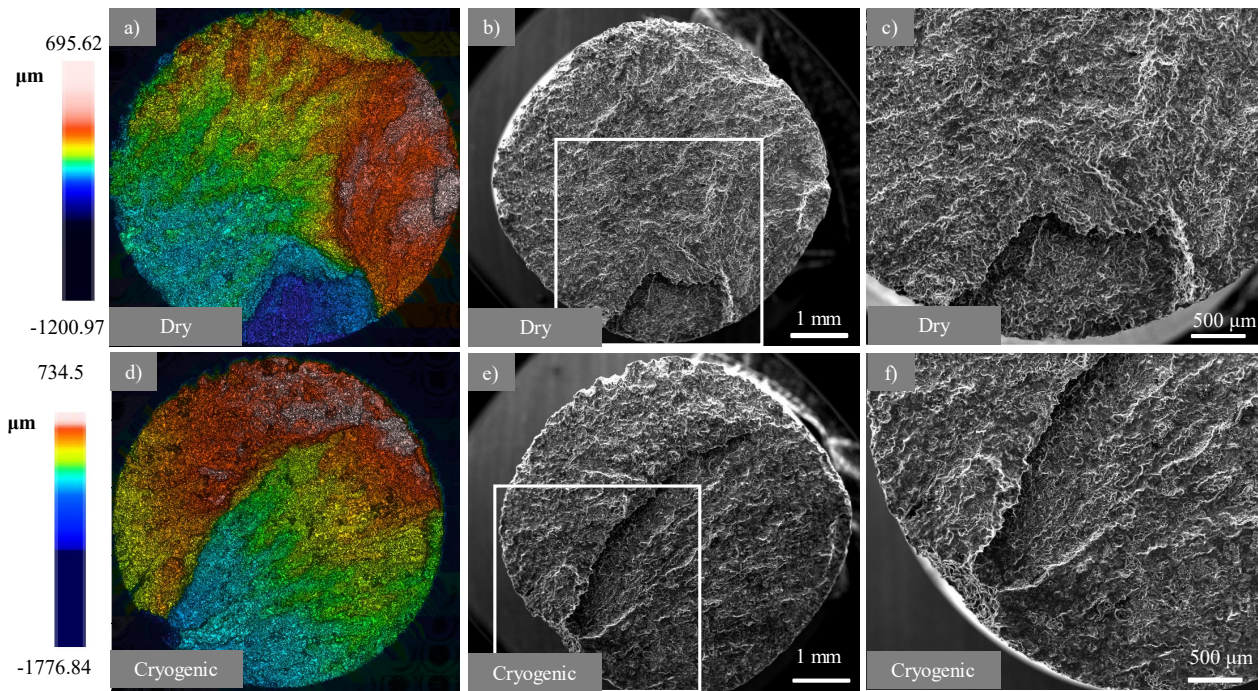
Figure 12 shows the comparison between the fracture surfaces after SSRT in SBF as a function of the machining cooling strategy. The topographies of the overall fracture surface (Figure 12 a and d) clearly demonstrated the sequence of the rupture. The large crack observed on the circumferential areas of the samples contributed considerably to the fracture: this crack propagated and, finally, when a critical SCC crack length was achieved, mechanical overloading took over, leading to the fracture of the sample. At a higher magnification (Figure 12 c and f), cleavage-like features and grain boundary cracking were observed, with a predominance of the former. Evidence of this is reported in Figure 13, where optical micrographs of the fractured specimens are reported.
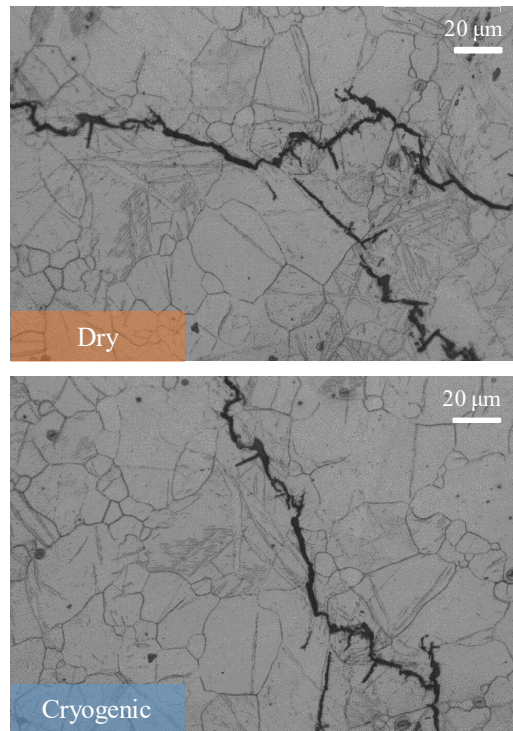
Figure 13. Optical micrographs of the AZ31 magnesium alloy after SSRTs in: a) dry; b) cryogenic conditions.

The fractographies of the specimens machined with different cooling strategies were similar, indicating that the susceptibility to SCC was independent of the application of liquid nitrogen. However, the tendency to pitting and localized corrosion at the sample circumference of the dry machined sample is considerably greater than that of the cryogenic machined one, as it can be seen from the tilted views of the gauge section of the samples reported in Figure 14. In fact, in the case of the dry sample, denser and deeper secondary cracks were evident, which contribute to a faster mechanical failure of the sample acting as stress concentrators.
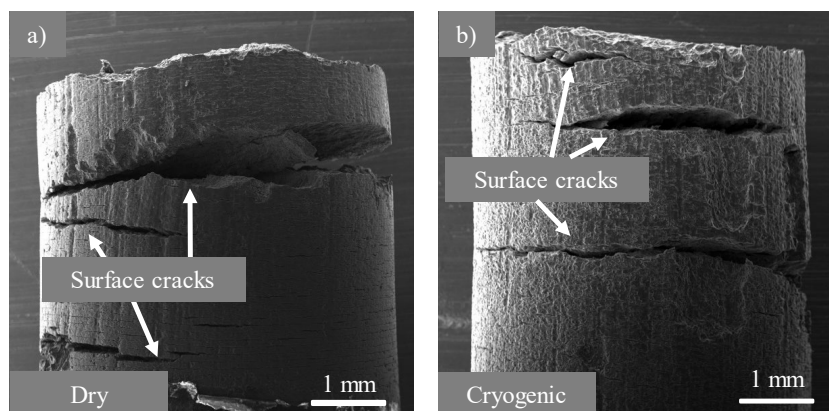
Fig.14. SEM fractographies of the gauge section of (a) dry and (b) cryogenic machined AZ31 samples after SSRTs in SBF.

4. Discussion

In this study, cryogenically machined samples have been proved to yield higher resistance to SCC in SBF compared to dry machined ones. The susceptibility indices I_{UTS} and I_ε of cryogenic machined samples were in fact decreased up to approximately 23% and 11%, respectively, compared to those of dry machined,

indicating a strengthened response to the synergistic application of mechanical load and corrosive environment. The examination of the fracture surfaces after SCCTs revealed that this improvement was not due to a different mechanism for corrosion crack propagation. The failure mechanisms of both dry and cryogenically machined samples are in fact a combination of transgranular and intergranular cracking, with a predominance of the former (Figures 11 and 13). The reasons of this improvement are instead based on the increase in corrosion resistance because of cryogenic machining. SCC of Mg alloys is widely attributed to the combination of two mechanisms, namely the anodic dissolution and cleavage-like fracture due to hydrogen embrittlement [53]. The rupture of the protective $Mg(OH)_2$ film due to the anodic dissolution or to mechanical loads allows the hydrogen evolved from the corrosion process to enter into the matrix and to embrittle the material, leading to a premature fracture [27]. In particular, pitting was reported as main precursor for the initiation of SCC cracks [54,55]. The reduced tendency to pitting and localized corrosion of the cryogenically machined samples (Figure 14) thus represents one of the reasons for the reduced SCC susceptibility, together with a lower corrosion rate (Figure 7). As the subsequent SCC crack propagation is governed by hydrogen embrittlement, and since hydrogen evolution is intimately associated with Mg dissolution (the dissolution of one Mg atom generates one hydrogen gas molecule [20]), a lower corrosion rate leads to a reduction of material embrittlement, and thus to a higher resistance to SCC.

The modified material corrosion performances are related to the machining-induced surface integrity changes. TEM analyses gathered in Figure 4 reported that the cryogenic treatment provides a surface nanolayer almost five times thicker than that after dry machining. These results agree with those obtained by Pu et al. reporting a wider nanocrystalline region in cryogenically machined AZ31B alloy than in the dry machined counterparts [45]. The wider extension of both the SPD and nano-crystalline layer in the case of cryogenic cooling can be explained as follows: during machining, the material is subjected to high strain at very high strain rate inducing the fragmentation of original grains by dislocation movements [56]. With the application of liquid nitrogen, this effect is emphasized since the temperature is greatly reduced. From a corrosion perspective, the thicker the nanocrystalline region, the lower the corrosion rate as nanoscale-sized grains reduce the corrosion rate [57,58] due to an accelerated formation of a passivating oxide film at grain boundaries [59]. An improved passive film renders the surface more electrochemically stable with a higher Electron Work Function (EWF), and the higher the EWF, the lower the corrosion rate.

The wider surface nanolayer induced by the cryogenic machining is not the only important variable that improves the corrosion resistance. As it can be seen from Figure 5, cryogenic machining induces a compressive state of stress, contrarily to what happened in dry machining. Residual stresses can usually be divided into the sum of two parts, one mechanically induced, and one thermally induced. During cutting, the material removal process itself is responsible for generating a compressive state on the workpiece, whereas the friction yields a tensile state of stress. However, the application of cryogenic cooling allows minimizing the tensile part of the residual stresses, leading to a compressive stress distribution at the machined surface. It is widely known that a tensile state of stress facilitates nucleation of micro-cracks as soon as corrosion is triggered [60,61], whereas compressive residual stresses are reported to increase the corrosion resistance. In particular, Denkena and Lucas reported the corrosion rate of a Mg-Ca alloy to be improved by a factor of approximately 100 [62]. The presence of a compressive state leads also to the formation and growth of a strengthened passive film since it narrows the interatomic distance of atoms, making the formation, growth and maintenance of the passive film easier [63]. Therefore, due to surface compressive residual stresses, the cryogenic machined samples showed lower corrosion current densities than the dry machined counterparts, leading to a superior ability to resist to the action of a mechanical loading in a corrosive environment.

Another reason for the improved corrosion resistance is surface texture. Although cryogenic machining was found to have no sensible influence on the surface roughness (Figure 6), a different effect was reported on the presence of surface defects. The density of tears in fact drastically increased in the case of the dry condition. Tears are machining defects usually attributed to the entrapment of chip particles or material

coming from the wear of the insert [64]. During cutting, these particles are dragged along the surface, causing scratches. In the case of cryogenic cooling, the wear of the tool is sensibly decreased due to the inhibition of the tool wear adhesion phenomena, a thermally activated mechanism. In addition, friction is reduced due to the increase of hardness of the mating interfaces compared to the dry condition [65]. This leads to a lower generation of particles coming from the wear of the tool, and therefore, less surface defects strengthening the resistance of the surface to corrosive attacks and reducing the SCC susceptibility.

5. Conclusions

In this study, the effect of cryogenic cooling during machining on the stress corrosion cracking (SCC) susceptibility of the AZ31 Mg alloy was assessed. SSRTs at a strain rate of $3.5 \cdot 10^{-6}$ s^{-1} were carried out in SBF at 37°C. In addition, potentiodynamic polarization tests, a full characterization of the surface integrity prior to testing and fracture surfaces analyses were carried out.

The main findings can be summarized as follows:

- Cryogenic machined samples were characterized by lower SCC susceptibility in SBF at body temperature than dry cut samples. This enhancement was attributed to the improved corrosion performances of the cryogenic machined samples due to the presence of a wider nanocrystalline layer, resulting in a faster formation of passivating surface oxides, and to the presence of compressive residual stresses instead of tensile.
- The analysis of the morphologies of the fracture surfaces after SSRTs proved that the use of liquid nitrogen during machining did not alter the AZ31 response mechanisms to SCC, being the fracture characterized by the presence of both intergranular and transgranular cracks, with the predominance of the latter. However, the analysis of both the fracture surface and the gauge section evidenced that cryogenic machined samples were less prone to pitting and localized corrosion, decreasing the SCC susceptibility.

It can be concluded that the cryogenic machining is an effective method to decrease the AZ31 sensitivity to SCC, and, therefore, can be considered a viable pathway for the fabrication of biodegradable implants with a prolonged durability inside the human body.

References

[1]   Ginebra, M.P., Traykova, T., Planell, J.A. (2006). Calcium phosphate cements as bone drug delivery systems: A review, J. Control. Release, 113(2), pp. 102–10, Doi: 10.1016/j.jconrel.2006.04.007.

[2]   Bradley, C., Harrison, J.E. (2004). Descriptive epidemiology of traumatic fractures in Australia, Australian Institute of Health and Welfare.

[3]   Chen, Q., Thouas, G.A. (2015). Metallic implant biomaterials, Mater. Sci. Eng. R Reports, 87, pp. 1–57, Doi: 10.1016/J.MSER.2014.10.001.

[4]   Hanawa, T. (2010).Overview of metals and applications. Metals for Biomedical Devices, Elsevier, pp. 3–24.

[5]   Albrektsson, T., Brånemark, P.-I., Hansson, H.-A., Lindström, J. (1981). Osseointegrated Titanium Implants: *Requirements for Ensuring a Long-Lasting, Direct Bone-to-Implant Anchorage in Man*, Acta Orthop. Scand., 52(2), pp. 155–70, Doi: 10.3109/17453678108991776.

[6]   Rossi, F., Lang, N.P., De Santis, E., Morelli, F., Favero, G., Botticelli, D. (2014). Bone-healing pattern at the surface of titanium implants: an experimental study in the dog, Clin. Oral Implants Res.,

25(1), pp. 124–31, Doi: 10.1111/clr.12097.

[7]   Bauer, T.W., Schils, J. (1999). The pathology of total joint arthroplasty.II. Mechanisms of implant failure., Skeletal Radiol., 28(9), pp. 483–97.

[8]   Dujovne, A.R., Bobyn, J.D., Krygier, J.J., Miller, J.E., Brooks, C.E. (1993). Mechanical compatibility of noncemented hip prostheses with the human femur, J. Arthroplasty, 8(1), pp. 7–22, Doi: 10.1016/S0883-5403(06)80102-6.

[9]   Engh, C.A., Bobyn, J.D. (1988). The influence of stem size and extent of porous coating on femoral bone resorption after primary cementless hip arthroplasty., Clin. Orthop. Relat. Res., (231), pp. 7–28.

[10] Kerner, J., Huiskes, R., van Lenthe, G.H., Weinans, H., van Rietbergen, B., Engh, C.A., Amis, A.A. (1999). Correlation between pre-operative periprosthetic bone density and post-operative bone loss in THA can be explained by strain-adaptive remodelling., J. Biomech., 32(7), pp. 695–703, Doi: 10.1016/S0021-9290(99)00041-X.

[11] Sumner, D.R., Galante, J.O. (1992). Determinants of stress shielding: design versus materials versus interface., Clin. Orthop. Relat. Res., (274), pp. 202–12.

[12] Turner, T.M., Sumner, D.R., Urban, R.M., Igloria, R., Galante, J.O. (1997). Maintenance of proximal cortical bone with use of a less stiff femoral component in hemiarthroplasty of the hip without cement. An investigation in a canine model at six months and two years., J. Bone Joint Surg. Am., 79(9), pp. 1381–90.

[13] Van Rietbergen, B., Huiskes, R., Weinans, H., Sumner, D.R., Turner, T.M., Galante, J.O. (1993). The mechanism of bone remodeling and resorption around press-fitted THA stems, J. Biomech., 26(4–5), pp. 369–82, Doi: 10.1016/0021-9290(93)90001-U.

[14] Wolff, J. (1986). The Law of Bone Remodelling, Berlin, Heidelberg, Springer Berlin Heidelberg.

[15] Pound, B.G. (2014). Corrosion behavior of metallic materials in biomedical applications . I . Ti and its alloys, 32, pp. 1–20, Doi: 10.1515/corrrev-2014-0007.

[16] Pound, B.G. (2014). Corrosion behavior of metallic materials in biomedical applications . II . Stainless steels and Co-Cr alloys, 32, pp. 21–41, Doi: 10.1515/corrrev-2014-0008.

[17] Jacobs, J.J., Gilbert, J.L., Urban, R.M. (1998). Corrosion of metal orthopaedic implants., J. Bone Joint Surg. Am., 80(2), pp. 268–82.

[18] Jacobs, J.J., Hallab, N.J., Skipor, A.K., Urban, R.M. (2003). Metal degradation products: a cause for concern in metal-metal bearings?, Clin. Orthop. Relat. Res., (417), pp. 139–47, Doi: 10.1097/01.blo.0000096810.78689.62.

[19] Beech, I.B., Sunner, J.A., Arciola, C.R., Cristiani, P. (2006). Microbially-influenced corrosion: damage to prostheses, delight for bacteria., Int. J. Artif. Organs, 29(4), pp. 443–52.

[20] Peron, M., Torgersen, J., Berto, F. (2017). Mg and Its Alloys for Biomedical Applications: Exploring Corrosion and Its Interplay with Mechanical Failure, Metals (Basel)., 7(7), pp. 252, Doi: 10.3390/met7070252.

[21] Li, N., Zheng, Y. (2013). Novel Magnesium Alloys Developed for Biomedical Application: A Review, J. Mater. Sci. Technol., 29(6), pp. 489–502, Doi: 10.1016/J.JMST.2013.02.005.

[22] Singh Raman, R.K., Jafari, S., Harandi, S.E. (2015). Corrosion fatigue fracture of magnesium alloys in bioimplant applications: A review, Eng. Fract. Mech., 137, pp. 97–108, Doi: 10.1016/j.engfracmech.2014.08.009.

[23] Staiger, M.P., Pietak, A.M., Huadmai, J., Dias, G. (2006). Magnesium and its alloys as orthopedic biomaterials: A review, Biomaterials, 27, pp. 1728–34, Doi: 10.1016/j.biomaterials.2005.10.003.

[24] Hänzi, A.C., Sologubenko, A.S., Uggowitzer, P.J. (2009). Design strategy for new biodegradable Mg–Y–Zn alloys for medical applications, ,.

[25] Teoh, S.. (2000). Fatigue of biomaterials: a review, Int. J. Fatigue, 22(10), pp. 825–37, Doi: 10.1016/S0142-1123(00)00052-9.

[26] Akahori, T., Niinomi, M., Fukunaga, K.-I., Inagaki, I. (2000). Effects of microstructure on the short fatigue crack initiation and propagation characteristics of biomedical α/β titanium alloys, Metall. Mater. Trans. A, 31(8), pp. 1949–58, Doi: 10.1007/s11661-000-0222-z.

[27] Jafari, S., Harandi, S.E., Singh Raman, R.K. (2015). A review of stress-corrosion cracking and corrosion fatigue of magnesium alloys for biodegradable implant applications, Jom, 67(5), pp. 1143–53, Doi: 10.1007/s11837-015-1366-z.

[28] Antunes, R.A., de Oliveira, M.C.L. (2012). Corrosion fatigue of biomedical metallic alloys: Mechanisms and mitigation, Acta Biomater., 8(3), pp. 937–62, Doi: 10.1016/j.actbio.2011.09.012.

[29] Jafari, S., Raman, R.K.S., Davies, C.H.J., Hofstetter, J., Uggowitzer, P.J., Löffler, J.F. (2017). Stress corrosion cracking and corrosion fatigue characterisation of MgZn1Ca0.3 (ZX10) in a simulated physiological environment, J. Mech. Behav. Biomed. Mater., 65, pp. 634–43, Doi: 10.1016/J.JMBBM.2016.09.033.

[30] Kannan, M.B., Raman, R.K.S. (2008). In vitro degradation and mechanical integrity of calcium-containing magnesium alloys in modified-simulated body fluid, Biomaterials, 29(15), pp. 2306–14, Doi: 10.1016/J.BIOMATERIALS.2008.02.003.

[31] Jafari, S., Raman, R.K.S., Davies, C.H.J. (2018). Stress corrosion cracking of an extruded magnesium alloy (ZK21) in a simulated body fluid, Eng. Fract. Mech., 201, pp. 47–55, Doi: 10.1016/J.ENGFRACMECH.2018.09.002.

[32] Mohajernia, S., Pour-Ali, S., Hejazi, S., Saremi, M., Kiani-Rashid, A.-R. (2018). Hydroxyapatite coating containing multi-walled carbon nanotubes on AZ31 magnesium: Mechanical-electrochemical degradation in a physiological environment, Ceram. Int., 44(7), pp. 8297–305, Doi: 10.1016/J.CERAMINT.2018.02.015.

[33] Chen, L., Sheng, Y., Zhou, H., Li, Z., Wang, X., Li, W. (2018). Influence of a MAO + PLGA coating on biocorrosion and stress corrosion cracking behavior of a magnesium alloy in a physiological environment, Corros. Sci., , Doi: 10.1016/J.CORSCI.2018.12.005.

[34] Gao, Y., Yerokhin, A., Matthews, A. (2015). Mechanical behaviour of cp-magnesium with duplex hydroxyapatite and PEO coatings, Mater. Sci. Eng. C, 49, pp. 190–200, Doi: 10.1016/J.MSEC.2014.12.081.

[35] Bobby Kannan, M., Dietzel, W., Blawert, C., Atrens, A., Lyon, P. (2008). Stress corrosion cracking of rare-earth containing magnesium alloys ZE41, QE22 and Elektron 21 (EV31A) compared with AZ80, Mater. Sci. Eng. A, 480(1–2), pp. 529–39, Doi: 10.1016/J.MSEA.2007.07.070.

[36] Choudhary, L., Singh Raman, R.K., Hofstetter, J., Uggowitzer, P.J. (2014). In-vitro characterization of stress corrosion cracking of aluminium-free magnesium alloys for temporary bio-implant applications, Mater. Sci. Eng. C, 42, pp. 629–36, Doi: 10.1016/J.MSEC.2014.06.018.

[37] Rim, K.T., Koo, K.H., Park, J.S. (2013). Toxicological Evaluations of Rare Earths and Their Health Impacts to Workers: A Literature Review, Saf. Health Work, 4(1), pp. 12–26, Doi: 10.5491/SHAW.2013.4.1.12.

[38] Ratna Sunil, B., Sampath Kumar, T.S., Chakkingal, U., Nandakumar, V., Doble, M., Devi Prasad, V., Raghunath, M. (2016). In vitro and in vivo studies of biodegradable fine grained AZ31 magnesium alloy produced by equal channel angular pressing, Mater. Sci. Eng. C, 59, pp. 356–67, Doi: 10.1016/J.MSEC.2015.10.028.

[39] Zhang, F., Ma, A., Jiang, J., Xu, H., Song, D., Lu, F., Nishida, Y. (2013). Enhanced biodegradation behavior of ultrafine-grained ZE41A magnesium alloy in Hank's solution, Prog. Nat. Sci. Mater. Int., 23(4), pp. 420–4, Doi: 10.1016/J.PNSC.2013.06.003.

[40] Xie, Q., Ma, A., Jiang, J., Cheng, Z., Song, D., Yuan, Y., Liu, H., Xie, Q., Ma, A., Jiang, J., Cheng, Z., Song, D., Yuan, Y., Liu, H. (2017). Stress Corrosion Cracking Behavior of Fine-Grained AZ61 Magnesium Alloys Processed by Equal-Channel Angular Pressing, Metals (Basel)., 7(9), pp. 343, Doi: 10.3390/met7090343.

[41] Mostaed, E., Fabrizi, A., Dellasega, D., Bonollo, F., Vedani, M. (2015). Microstructure, mechanical behavior and low temperature superplasticity of ECAP processed ZM21 Mg alloy, J. Alloys Compd., 638, pp. 267–76, Doi: 10.1016/J.JALLCOM.2015.03.029.

[42] Bertolini, R., Bruschi, S., Ghiotti, A. (2018). Large Strain Extrusion Machining under Cryogenic Cooling to Enhance Corrosion Resistance of Magnesium Alloys for Biomedical Applications, Procedia Manuf., 26, pp. 217–27, Doi: 10.1016/J.PROMFG.2018.07.030.

[43] Pu, Z., Outeiro, J.C., Batista, A.C., Dillon, O.W., Puleo, D.A., Jawahir, I.S. (2011). Surface Integrity in Dry and Cryogenic Machining of AZ31B Mg Alloy with Varying Cutting Edge Radius Tools, Procedia Eng., 19, pp. 282–7, Doi: 10.1016/J.PROENG.2011.11.113.

[44] Jawahir, I.S., Puleo, D.A., Schoop, J. (2016). Cryogenic Machining of Biomedical Implant Materials for Improved Functional Performance, Life and Sustainability, Procedia CIRP, 46, pp. 7–14, Doi: 10.1016/J.PROCIR.2016.04.133.

[45] Pu, Z., Dillon, O.W., Puelo, D.A., Jawahir, I.S. (2015). Cryogenic machining and burnishing of magnesium alloys to improve in vivo corrosion resistance, Surf. Modif. Magnes. Its Alloy. Biomed. Appl., , pp. 103–33, Doi: 10.1016/B978-1-78242-078-1.00005-0.

[46] Bruschi, S., Bertolini, R., Ghiotti, A., Savio, E., Guo, W., Shivpuri, R. (2018). Machining-induced surface transformations of magnesium alloys to enhance corrosion resistance in human-like environment, CIRP Ann., 67(1), pp. 579–82, Doi: 10.1016/J.CIRP.2018.04.040.

[47] Bertolini, R., Bruschi, S., Ghiotti, A., Pezzato, L., Dabalà, M. (2017). The Effect of Cooling Strategies and Machining Feed Rate on the Corrosion Behavior and Wettability of AZ31 Alloy for Biomedical Applications, Procedia CIRP, 65, pp. 7–12, Doi: 10.1016/J.PROCIR.2017.03.168.

[48] Kokubo, T., Takadama, H. (2006). How useful is SBF in predicting in vivo bone bioactivity?, Biomaterials, 27(15), pp. 2907–15, Doi: 10.1016/J.BIOMATERIALS.2006.01.017.

[49] Choudhary, L., Raman, R.K.S. (2011). Acta Biomaterialia Magnesium alloys as body implants : Fracture mechanism under dynamic and static loadings in a physiological environment, Acta Biomater., 8(2), pp. 916–23, Doi: 10.1016/j.actbio.2011.10.031.

[50] Thirumalaikumarasamy, D., Shanmugam, K., Balasubramanian, V. (2014). Comparison of the corrosion behaviour of AZ31B magnesium alloy under immersion test and potentiodynamic polarization test in NaCl solution, J. Magnes. Alloy., 2(1), pp. 36–49, Doi: 10.1016/J.JMA.2014.01.004.

[51] Bruschi, S., Pezzato, L., Ghiotti, A., Dabalà, M., Bertolini, R. (2019). Effectiveness of using low-temperature coolants in machining to enhance durability of AISI 316L stainless steel for reusable biomedical devices, J. Manuf. Process., 39, pp. 295–304, Doi: 10.1016/J.JMAPRO.2019.02.003.

[52] Şerban, D.A., Marsavina, L., Rusu, L., Negru, R. (2019). Numerical study of the behavior of magnesium alloy AM50 in tensile and torsional loadings, Arch. Appl. Mech., 89(5), pp. 911–7, Doi: 10.1007/s00419-018-1492-5.

[53] Winzer, N., Atrens, A., Song, G., Ghali, E., Dietzel, W., Kainer, K.U., Hort, N., Blawert, C. (2005). A critical review of the Stress Corrosion Cracking (SCC) of magnesium alloys, Adv. Eng. Mater.,

7(8), pp. 659–93, Doi: 10.1002/adem.200500071.

[54]   Stampella, R.S., Procter, R.P.M., Ashworth, V. (1984). Environmentally-induced cracking of magnesium, Corros. Sci., 24(4), pp. 325–41, Doi: 10.1016/0010-938X(84)90017-9.

[55]   Raja, V.S., Padekar, B.S. (2013). Role of chlorides on pitting and hydrogen embrittlement of Mg–Mn wrought alloy, Corros. Sci., 75, pp. 176–83, Doi: 10.1016/J.CORSCI.2013.05.030.

[56]   Shen, N., Ding, H., Pu, Z., Jawahir, I.S., Jia, T. (2017). Enhanced Surface Integrity From Cryogenic Machining of AZ31B Mg Alloy: A Physics-Based Analysis With Microstructure Prediction, J. Manuf. Sci. Eng., 139(6), pp. 061012, Doi: 10.1115/1.4034279.

[57]   Hamu, G. Ben., Eliezer, D., Wagner, L. (2009). The relation between severe plastic deformation microstructure and corrosion behavior of AZ31 magnesium alloy, J. Alloys Compd., 468(1–2), pp. 222–9, Doi: 10.1016/J.JALLCOM.2008.01.084.

[58]   Liu, Y., Liu, D., You, C., Chen, M. (2015). Effects of grain size on the corrosion resistance of pure magnesium by cooling rate-controlled solidification, Front. Mater. Sci., 9(3), pp. 247–53, Doi: 10.1007/s11706-015-0299-3.

[59]   Witte, F., Hort, N., Vogt, C., Cohen, S., Kainer, K.U., Willumeit, R., Feyerabend, F. (2008). Degradable biomaterials based on magnesium corrosion, Curr. Opin. Solid State Mater. Sci., 12(5), pp. 63–72, Doi: 10.1016/j.cossms.2009.04.001.

[60]   Sano, Y., Obata, M., Kubo, T., Mukai, N., Yoda, M., Masaki, K., Ochi, Y. (2006). Retardation of crack initiation and growth in austenitic stainless steels by laser peening without protective coating, Mater. Sci. Eng. A, 417(1–2), pp. 334–40, Doi: 10.1016/J.MSEA.2005.11.017.

[61]   Brinksmeier, E., Cammett, J.T., König, W., Leskovar, P., Peters, J., Tönshoff, H.K. (1982). Residual Stresses — Measurement and Causes in Machining Processes, CIRP Ann., 31(2), pp. 491–510, Doi: 10.1016/S0007-8506(07)60172-3.

[62]   Denkena, B., Lucas, A. (2007). Biocompatible Magnesium Alloys as Absorbable Implant Materials – Adjusted Surface and Subsurface Properties by Machining Processes, CIRP Ann., 56(1), pp. 113–6, Doi: 10.1016/J.CIRP.2007.05.029.

[63]   Liu, X., Frankel, G.S. (2006). Effects of compressive stress on localized corrosion in AA2024-T3, Corros. Sci., 48(10), pp. 3309–29, Doi: 10.1016/J.CORSCI.2005.12.003.

[64]   Ginting, A., Nouari, M. (2009). Surface integrity of dry machined titanium alloys, Int. J. Mach. Tools Manuf., 49(3–4), pp. 325–32, Doi: 10.1016/J.IJMACHTOOLS.2008.10.011.

[65]   Bordin, A., Bruschi, S., Ghiotti, A., Bariani, P.F. (2015). Analysis of tool wear in cryogenic machining of additive manufactured Ti6Al4V alloy, Wear, 328–329, pp. 89–99, Doi: 10.1016/J.WEAR.2015.01.030.